Chapter 5

Coronal Elemental Abundance Analysis: FIP and Inverse-FIP effect

In this chapter, we investigate the variation in elemental abundances within the coronal plasma during flares observed on two active stars, AB Dor and HR 1099. By comparing the coronal abundances to solar photospheric values, we identify clear signatures of the inverse-FIP effect in both stars, which shows an inverse effect in comparison to the effect usually observed in the Sun. To conduct this analysis, we employ high-resolution X-ray spectroscopy using data from the Reflection Grating Spectrometer (RGS) onboard the XMM-Newton observatory, which provides the spectral resolution necessary to distinguish individual elemental spectral lines. Additionally, we explore the strength of the inverse-FIP effect using the Fe/O abundance ratio as a diagnostic indicator. It was found to be varying in the range 0.02-0.04 from quiescent to flare segments for these stars, showing the varying strength of the i-FIP effect. A detailed comparison with previous studies has supported the observed fractionation in coronal abundances in these active stars.

5.1 FIP and Inverse-FIP Effect

Due to fractionation processes associated with the first ionization potential (FIP), the elemental abundances in stellar coronae often differ from those in the underlying photosphere. In slow-rotating, less active stars such as the Sun, elements with FIP < 10 eV are typically enhanced relative to those with FIP > 10 eV, a phenomenon known as the FIP effect (Feldman, 1992; Feldman and Laming, 2000; Laming et al., 1995). In contrast, fast-rotating stars with higher magnetic activity frequently exhibit the inverse-FIP (i-FIP) effect, where high-FIP elements are relatively more abundant (see Laming, 2015, 2021). Additionally, some stars show no FIP bias at all, a characteristic linked to their magnetically inactive chromospheres (Drake et al., 1994). These effects are discussed in more detail in Chapter 1.

5.2 RGS Spectral Analysis

The high spectral resolution of the RGS spectrometers makes them suitable for detailed individual abundance analysis, which has been carried out in this chapter. The data used come from the observations described in Table 2.1 of Chapter 2. We used the standard data reduction method to create the quiescent and flare spectra, as also explained in Chapter 2.

5.2.1 AB Dor

For AB Dor, we analyzed the RGS spectra during both quiescent and flaring states using a 3-temperature VAPEC model to represent the thermal plasma, combined with the tbabs model to account for interstellar absorption (N_H). During the quiescent phase, the temperatures and emission measures were treated as free parameters, while the N_H value was fixed at 2×10^{18} cm^{-2}. The abundances of Aluminum (Al) and Nickel (Ni) were fixed to their

solar photospheric values. Other elemental abundances were allowed to vary but were tied among each temperature component.

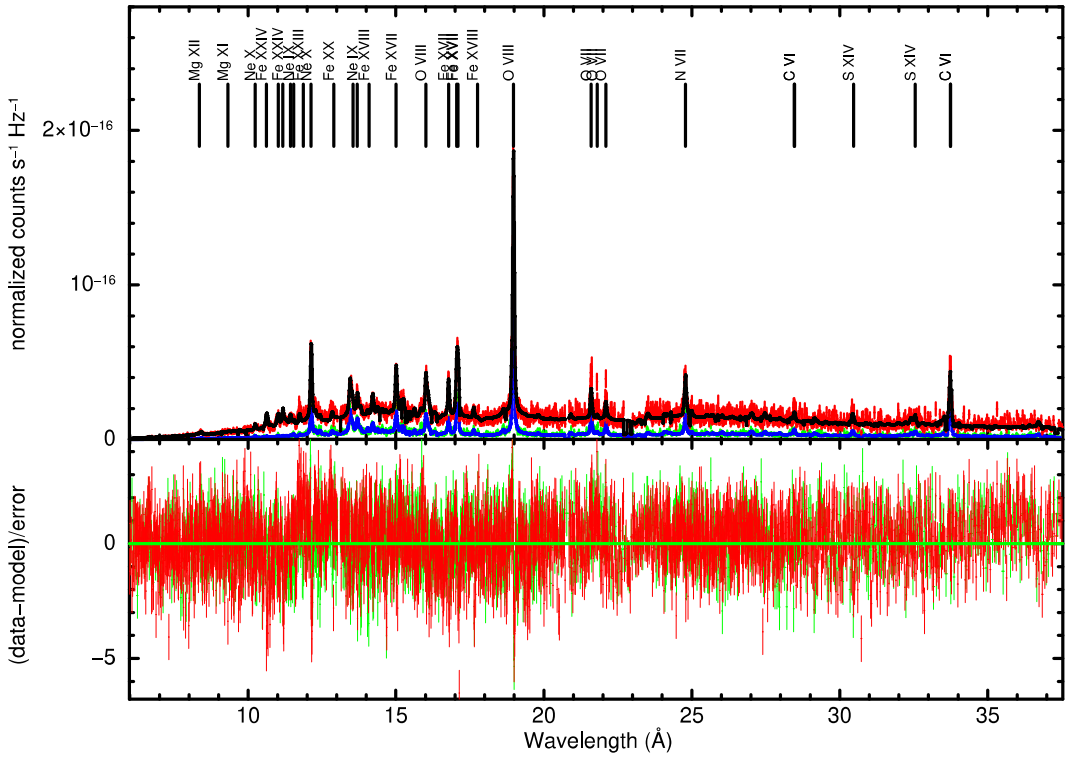

Figure 5.1: RGS spectra of AB Dor during quiescent (P11) and flaring state (F20) from the set S6 are shown in green and red color, respectively. The best fit 3-temperature VAPEC model along with the fi for both is shown in blue and black solid lines, respectively.

For the flaring state, a similar 3-T VAPEC model was applied. The first two temperatures (kT_1 and kT_2) and corresponding emission measures (EM_1 and EM_2) were fixed to the best-fit values obtained from the quiescent state, representing the underlying quiescent emission. The third component was used to model the flare and was allowed to vary. Abundances across all three components were tied together. In order to achieve a sufficient signal-to-noise ratio, the flare in RGS requires stronger re-binning for spectral analysis than for the PN. Therefore, rather than dividing the flare into different segments as done for the PN spectral analysis, we used the spectra of the entire flaring event to determine the spectral parameters. The best fit model parameters within a 68% confidence range are

given in Table 5.3 for both quiescent and flaring states of AB Dor. The best-fit preflare P11 and flare F20 spectra with the residual of the best-fit 3-T VAPEC model are also illustrated in Fig. 5.1. Moreover, all the modeled quiescent and flare spectra are illustrated in Fig. 5.3.

5.2.2 HR 1099

For HR 1099, we applied a similar approach as used for AB Dor. The RGS1 and RGS2 spectra for set A2 were generated for both the quiescent state (P4) and the flaring state (F3) and fitted with the VAPEC model. Additionally, the TBABS model was used to account for the N_H , which was fixed to a minimum value of 10^{18} cm^{-2}. All temperatures and corresponding emission measures were left as free parameters for the quiescent state spectral fitting. The abundances of He, Ni, and Al were set to the solar photospheric values, while the other abundances were allowed to vary and were tied among each temperature component. We found that a 3-T plasma model provided the best fit for the P4 quiescent segment. For the flaring spectra, a 4-T VAPEC model was used for the fitting. The first

three temperatures and corresponding normalization parameters were fixed at the quiescent values as obtained from spectral fitting of the P4 region, and all abundances were tied among the different components. Table 5.1 represents the best-fit model parameters for both the quiescent and flaring phases within a 68% confidence interval.

In Fig. 5.2, we present the RGS1 and RGS2 spectra of HR 1099 for flare F3 and its pre-flare state P4, including emission lines from various elements. The best-fit thermal plasma model, VAPEC, is illustrated with solid lines for both the flare and quiescent states. The residuals of the best-fit model are shown in the lower panel.

5.3 Results

The measured abundance as a function of FIP for the quiescent and flaring phases of different observations of AB Dor are shown in Fig. 5.4. The coronal abundances of

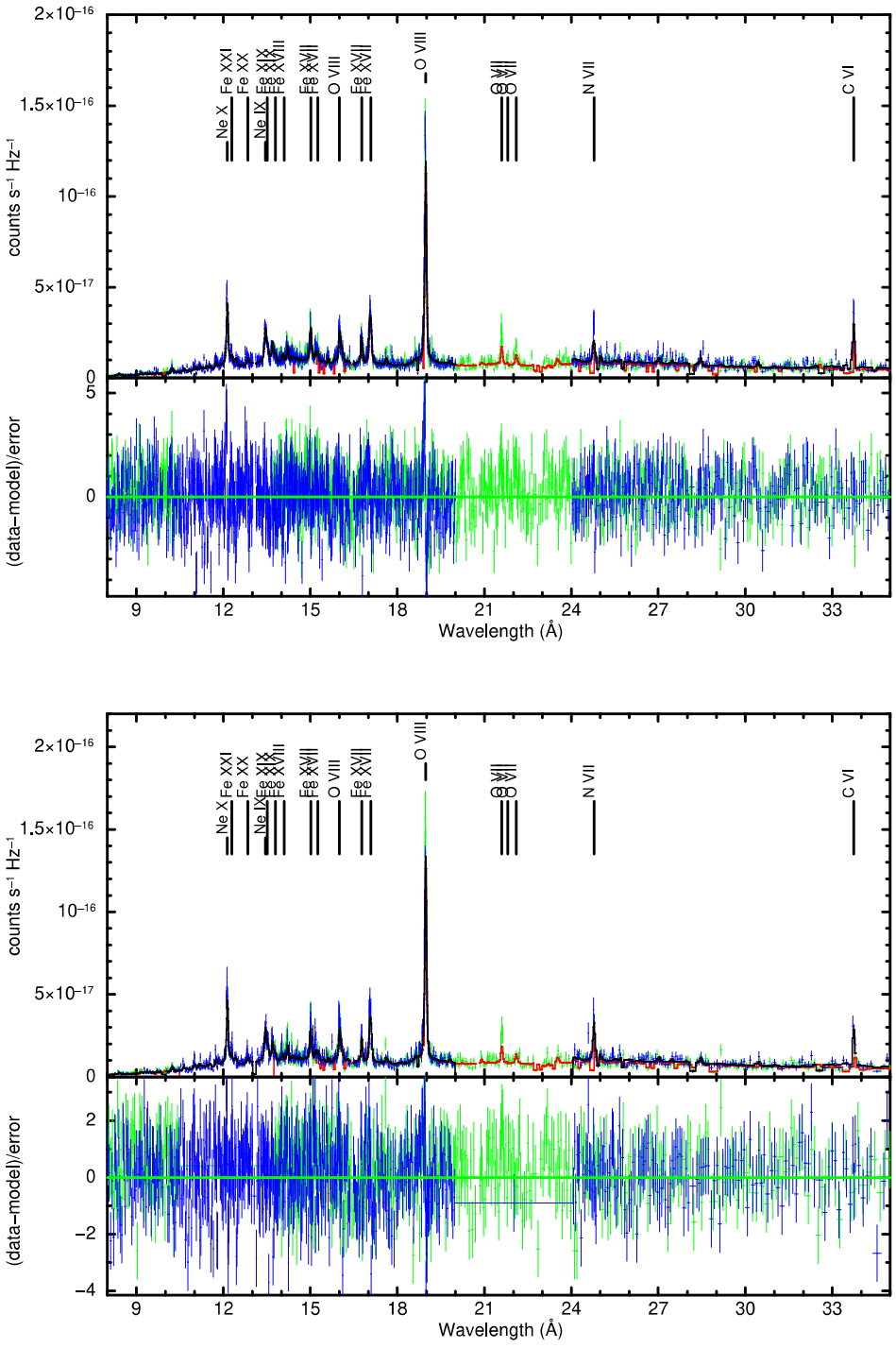

Figure 5.2: The RGS1 and RGS2 spectra of pre-flare state P4 and flare F3 for HR 1099 are shown in the upper panel with 3-T VAPEC and 4-T VAPEC models, respectively. The lower panel shows the residuals of the modeled spectra.

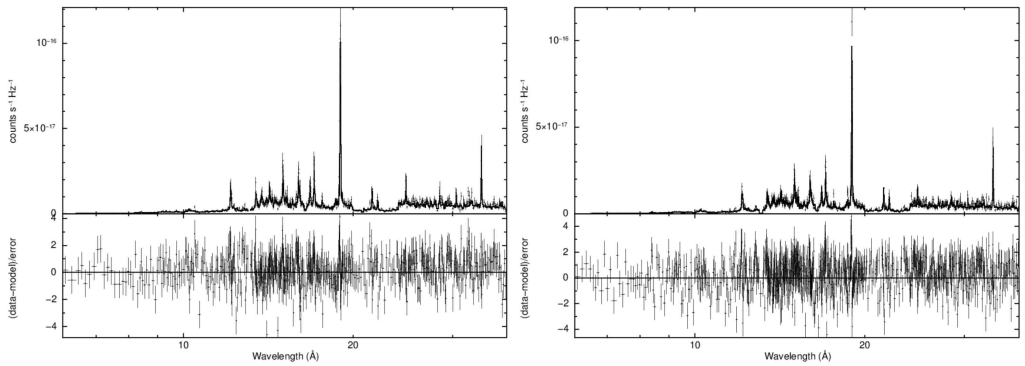

(a) F4

(b) F5

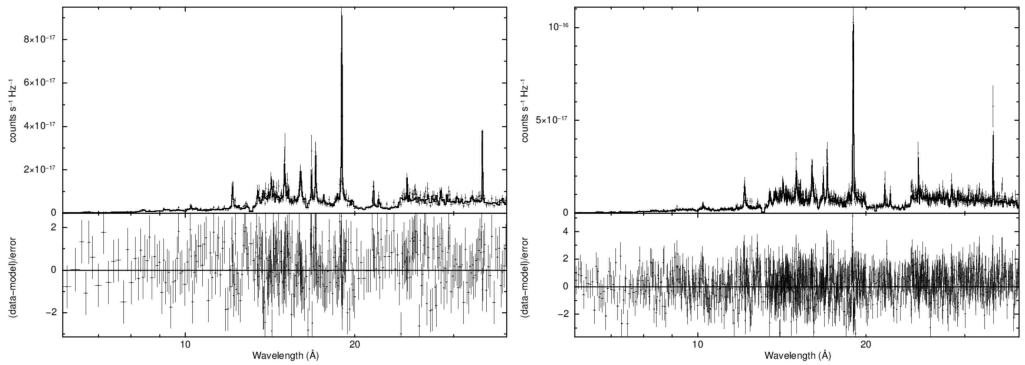

(c) F6

(d) F7

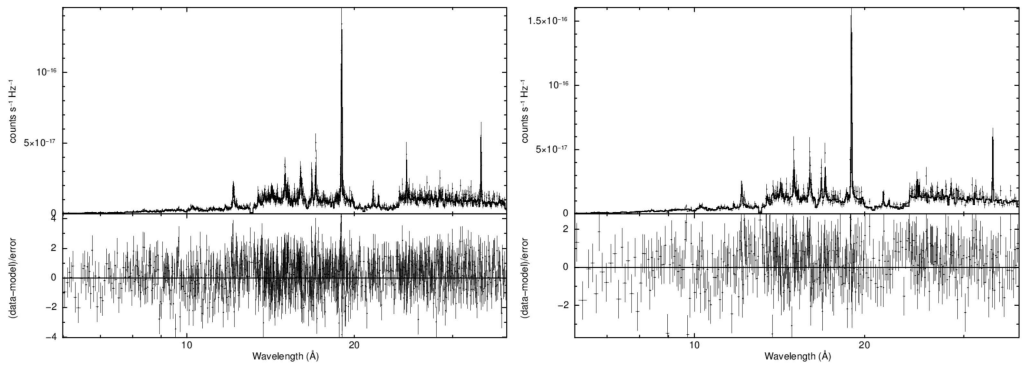

(e) F8

(f) F9

Figure 5.3: Modeled spectra of all the quiescent and flare segments.

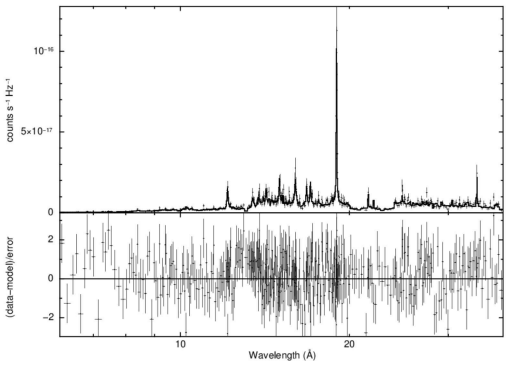

(g) F10

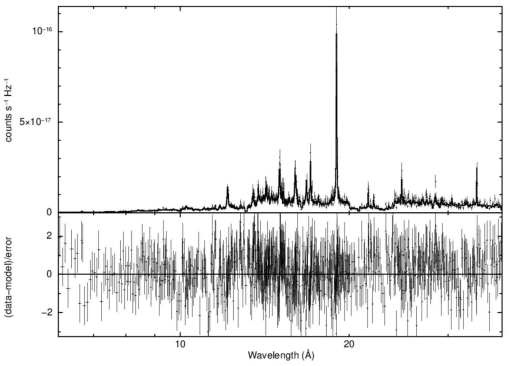

(h) F11

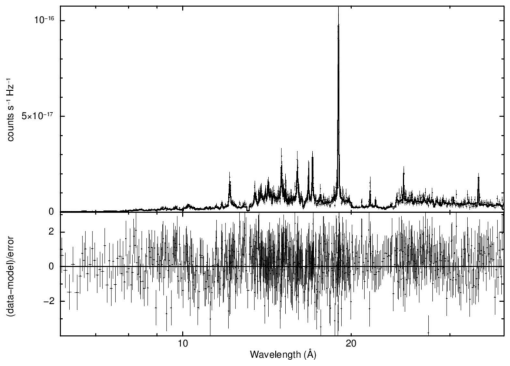

(i) F12

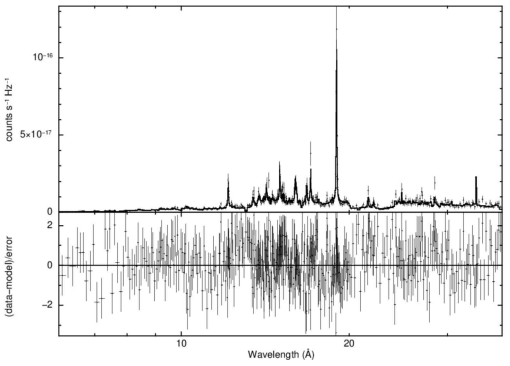

(j) F13

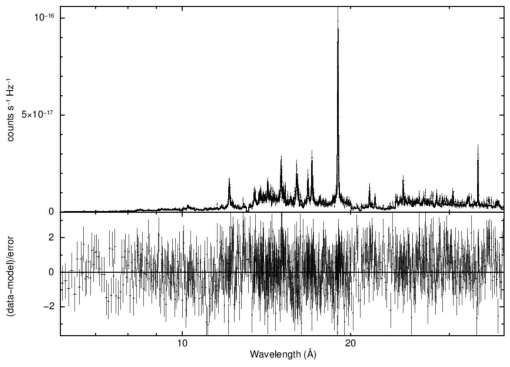

(k) F14

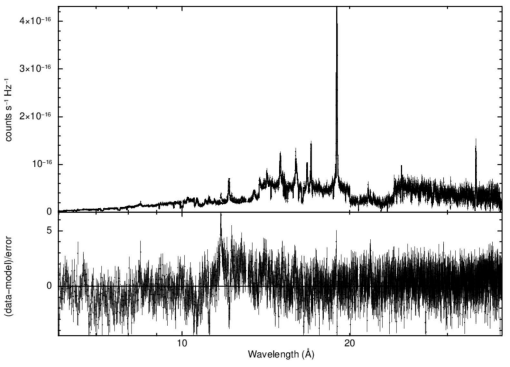

(l) F15

Figure 5.3: Continued...

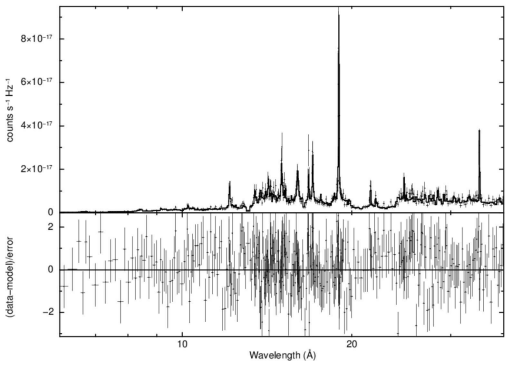

(m) F16

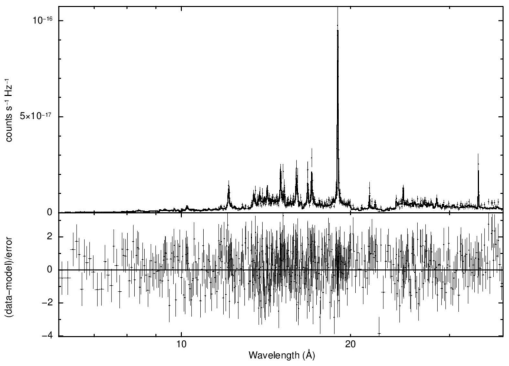

(n) F17

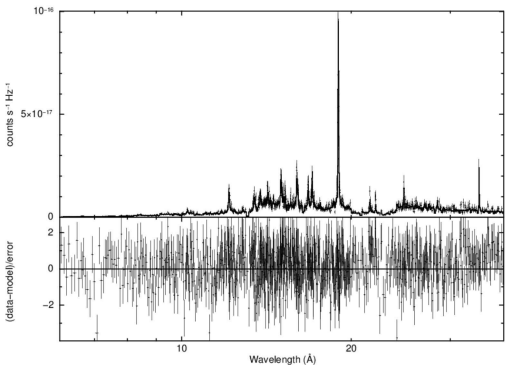

(o) F18

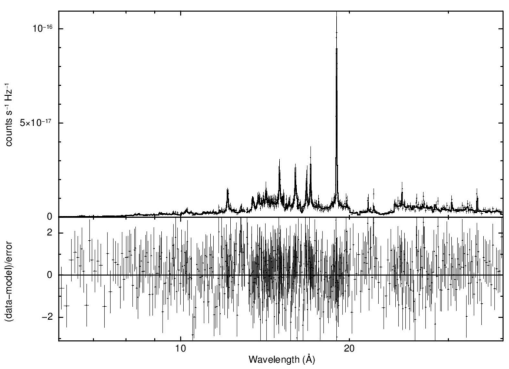

(p) F19

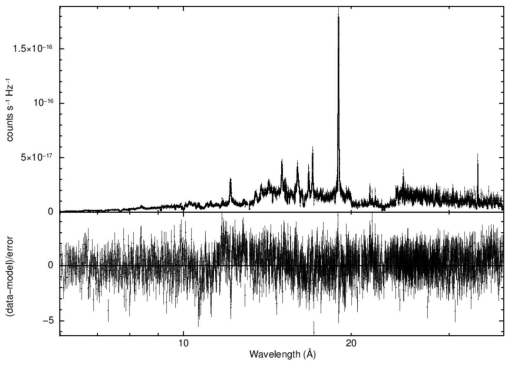

(q) F20

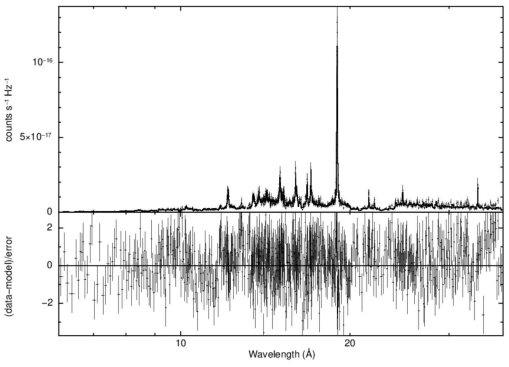

(r) F21

Figure 5.3: Continued...

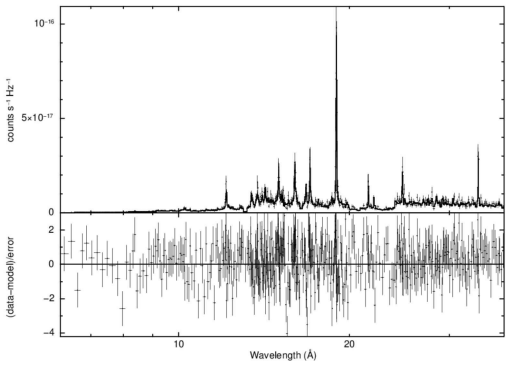

(s) P3

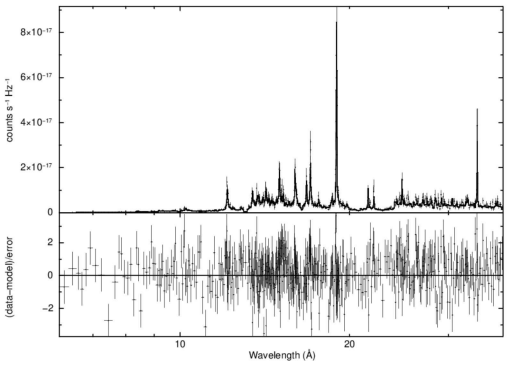

(t) P4

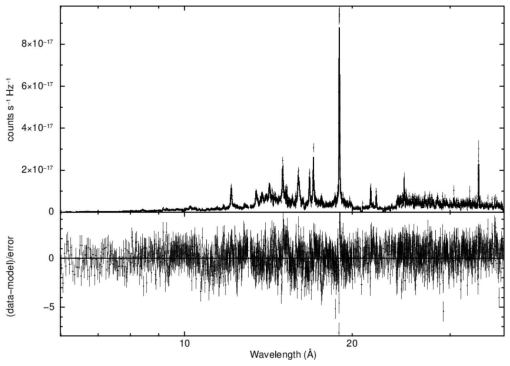

(u) P5

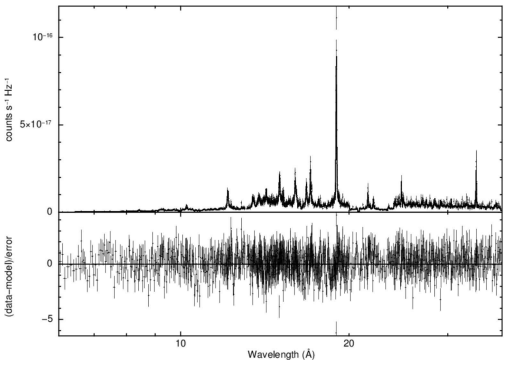

(v) P6

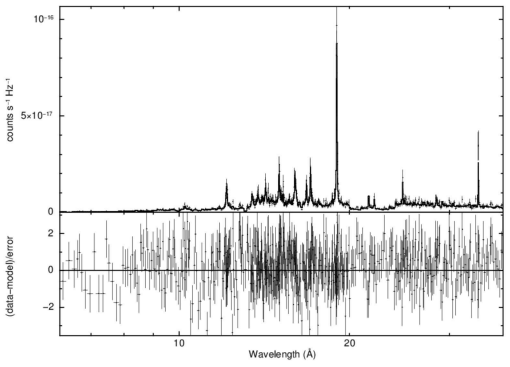

(w) P7

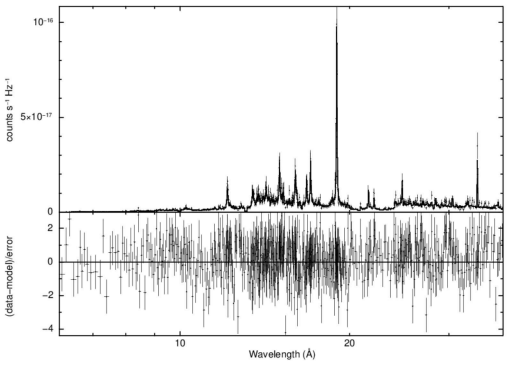

(x) P8

Figure 5.3: Continued...

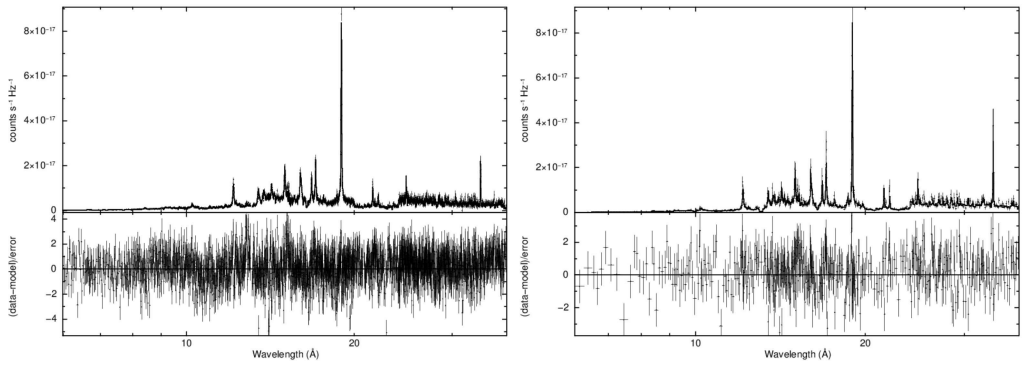

(y) P9 (z) P10

Figure 5.3: Continued...

elements Mg, Fe, and Si with FIP <10 eV are found to be under-abundant relative to solar photospheric values for both the quiescent and flaring states. The average abundance of Mg, Fe, and Si during quiescent states is found to be ~0.31, ~0.19, and ~0.42, respectively. Also, all other high FIP elements except Ne (with an average abundance of ~1.34) are found to be underabundant during quiescent states. Furthermore, our observations revealed the presence of the Inverse First Ionization Potential (I-FIP) effect during both quiescent and flaring states. In the majority of the flaring periods, the abundances of individual elements were observed to be higher compared to those in the quiescent state.

Moreover, in the case of HR 1099, the measured abundances as a function of FIP, for both quiescent and flaring phases, are shown in Fig. 5.5. The elements with FIP < 10 eV like Mg, Fe, and Si were found to be under-abundant relative to the solar photospheric values in both states, with values of approximately ~0.44, ~0.26, and ~0.70 for the quiescent state, and ~0.48, ~0.28, and ~0.86 for the flaring state, respectively. Additionally, the abundances of N, O, and Si are lower in the quiescent state compared to the flaring state, while the remaining abundances are similar to the flaring values within a 68% confidence interval. Thus, the evidence of the i-FIP effect is observed in HR 1099 in the case of both the quiescent and flaring states in the present observational baseline.

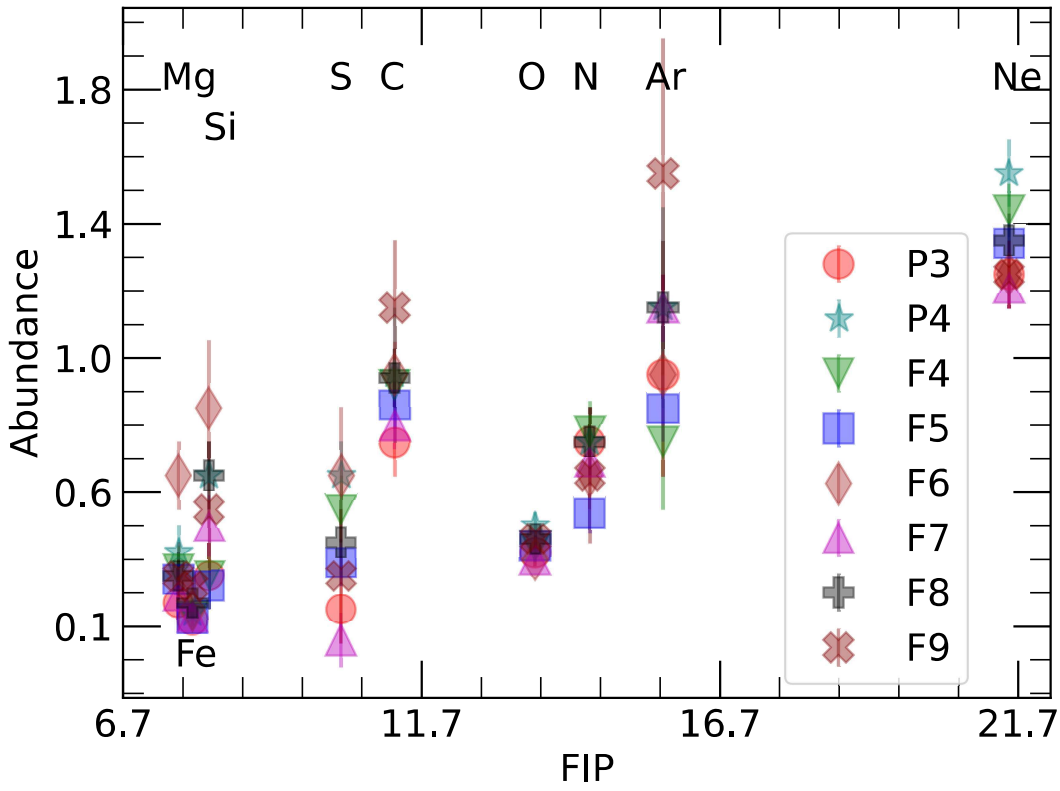

(a) Set 2

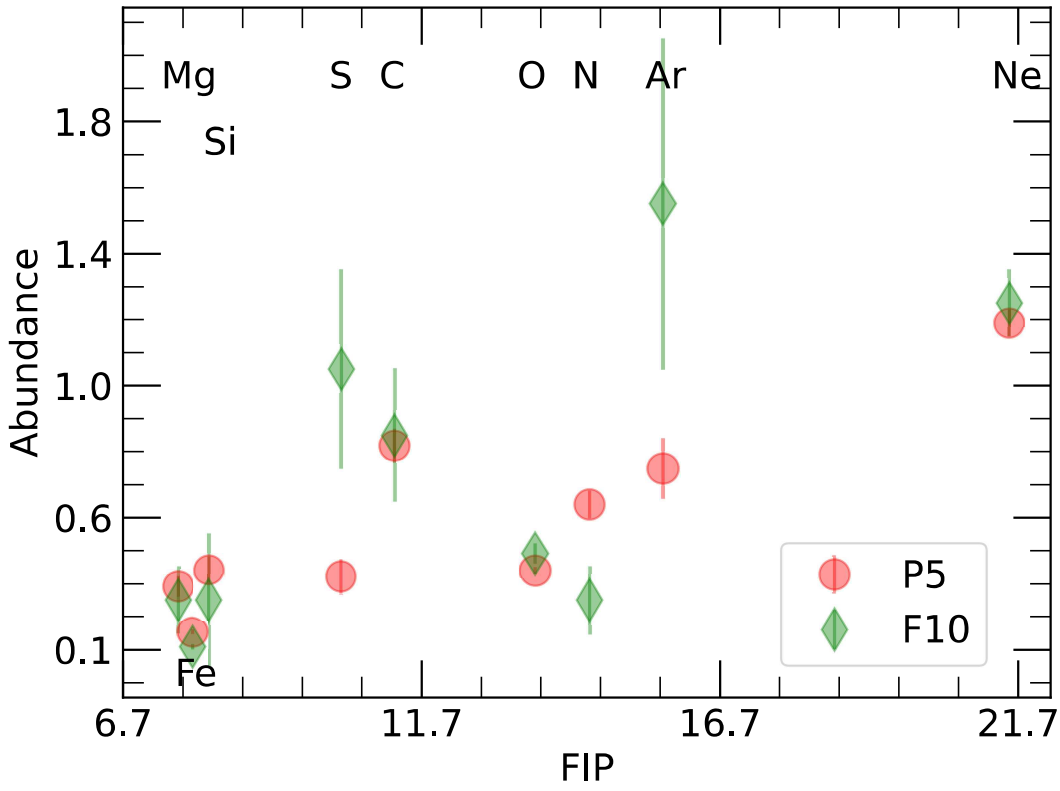

(b) Set 3

Figure 5.4: Elemental abundances plotted as a function of FIP for both quiescent and flaring states during different observations of AB Dor.

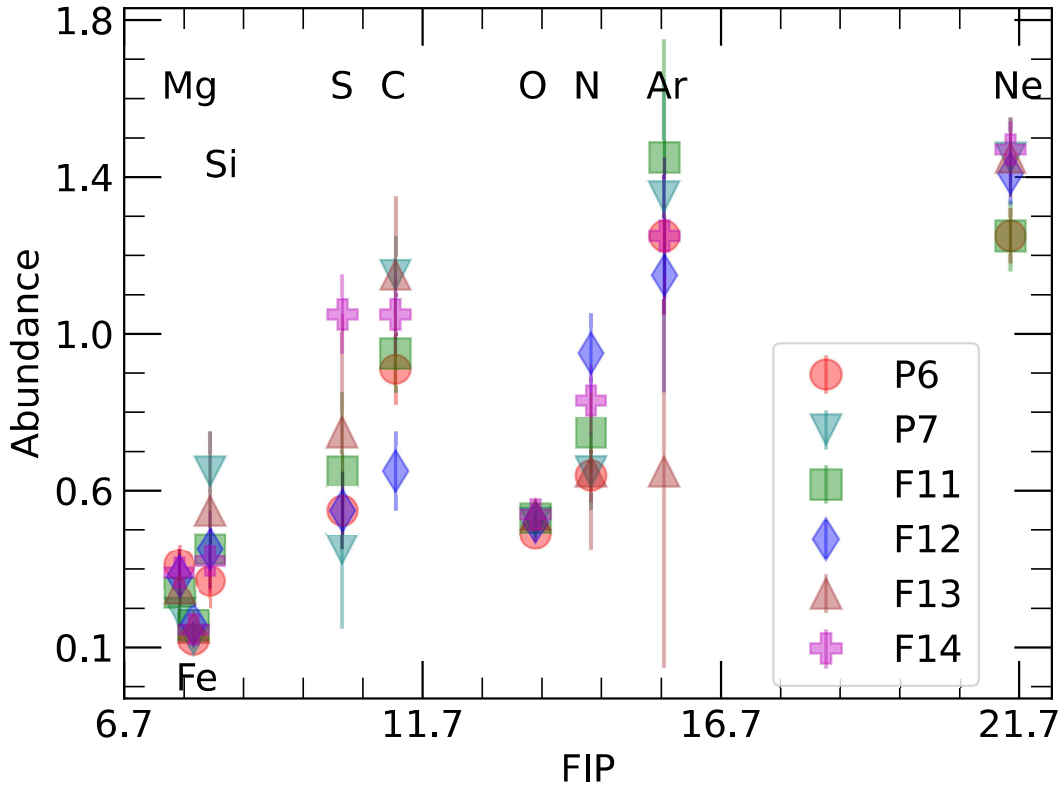

(c) Set 4

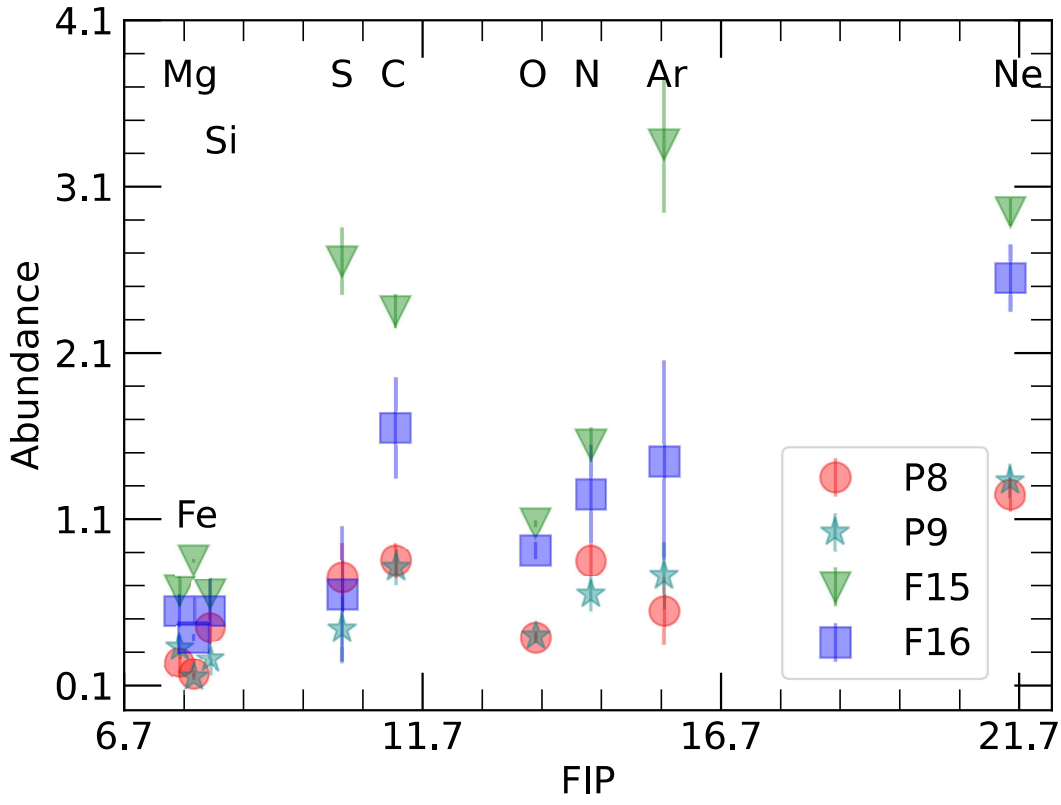

(d) Set 5

Figure 5.4: Continued...

Table 5.1: The best-fit optimal spectral parameters derived from fitting the RGS spectra within a 68% confidence level.

Segments (→)	P4	F3
Parameters (↓)	$Z/Z_{\odot}$	$Z/Z_{\odot}$
kT_1 (keV)	$0.39^{+0.01}_{-0.02}$	....
kT_2 (keV)	$0.83^{+0.01}_{-0.02}$	....
kT_3 (keV)	$1.74^{+0.05}_{-0.05}$	....
kT_4 (keV)	....	$1.9^{+1.4}_{-0.4}$
EM_1 (10^{53}cm^{-3})	$1.02^{+0.06}_{-0.09}$	....
EM_2 (10^{53}cm^{-3})	$2.27^{+0.09}_{-0.09}$	....
EM_3 (10^{53}cm^{-3})	$4.6^{+0.1}_{-0.1}$	....
EM_4 (10^{53}cm^{-3})	....	$1.08^{+0.05}_{-0.03}$
C	$1.0^{+0.1}_{-0.1}$	$1.1^{+0.1}_{-0.1}$
N	$0.55^{+0.09}_{-0.09}$	$0.95^{+0.07}_{-0.07}$
O	$0.72^{+0.03}_{-0.03}$	$0.79^{+0.01}_{-0.02}$
Ne	$1.50^{+0.08}_{-0.07}$	$1.63^{+0.07}_{-0.07}$
Mg	$0.44^{+0.05}_{-0.05}$	$0.48^{+0.04}_{-0.04}$
Si	$0.70^{+0.07}_{-0.07}$	$0.86^{+0.07}_{-0.07}$
S	$0.38^{+0.1}_{-0.09}$	$0.49^{+0.09}_{-0.09}$
Ar	$0.9^{+0.2}_{-0.2}$	$1.3^{+0.2}_{-0.2}$
Fe	$0.26^{+0.01}_{-0.01}$	$0.28^{+0.04}_{-0.04}$
χ^2_{ν}	1.41	1.19
(dof)	2502	1249

Note. All the elemental abundances are in terms of solar photospheric abundances taken from Wilms et al. (2000).

5.4 Discussion and Conclusions

The elemental coronal abundances add extra information to the physical nature of the corona of active stars. In case of AB Dor, the abundance of the majority of elements was found to be underabundant during the quiescent with respect to the solar photospheric values. However, the abundance of Ne in the quiescent state was found to be more than the solar photospheric value. As the solar photospheric Ne abundances are much uncertain due to the lack of photospheric absorption lines, so, Ne is usually quoted with reference to some other high FIP elements like oxygen, whose photospheric values are well constrained. Here, by assuming the photospheric values of AB Dor similar to the solar photospheric

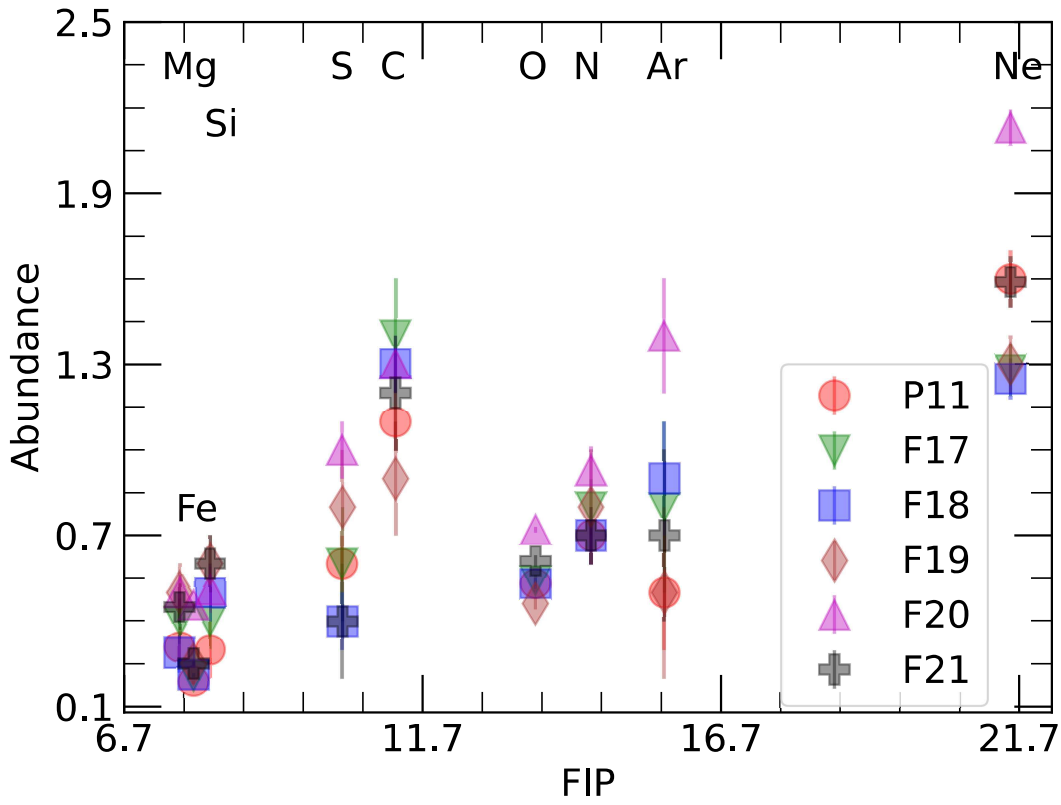

(e) Set 6

Figure 5.4: Continued...

values (Wood et al., 2018), we noticed during the flares $(Ne/O)_*$ ratio ranges from 0.34 to 0.52, whereas the average quiescent value is 0.44 with a minimum of 0.39 and a maximum of 0.48, which is similar to the values reported by Drake and Testa (2005) for the active stars. Although the FIP effect observed with this assumption was challenged in some cases (studied in detail by Sanz-Forcada et al., 2004). Moreover, the individual abundances during both the quiescent and flaring states in the coronal loops of HR 1099 are also found to exhibit a similar i-FIP effect. The abundance study of the corona of HR 1099 using high-resolution spectroscopy in X-ray domain has been performed by various authors in the past, showing the presence of the i-FIP effect in the corona of this star using various plasma models like CIE, MEKAL, APEC etc. (Bozzo et al., 2024; den Herder et al., 2001; Huenemoerder et al., 2013; Osten et al., 2004; Seli et al., 2022).

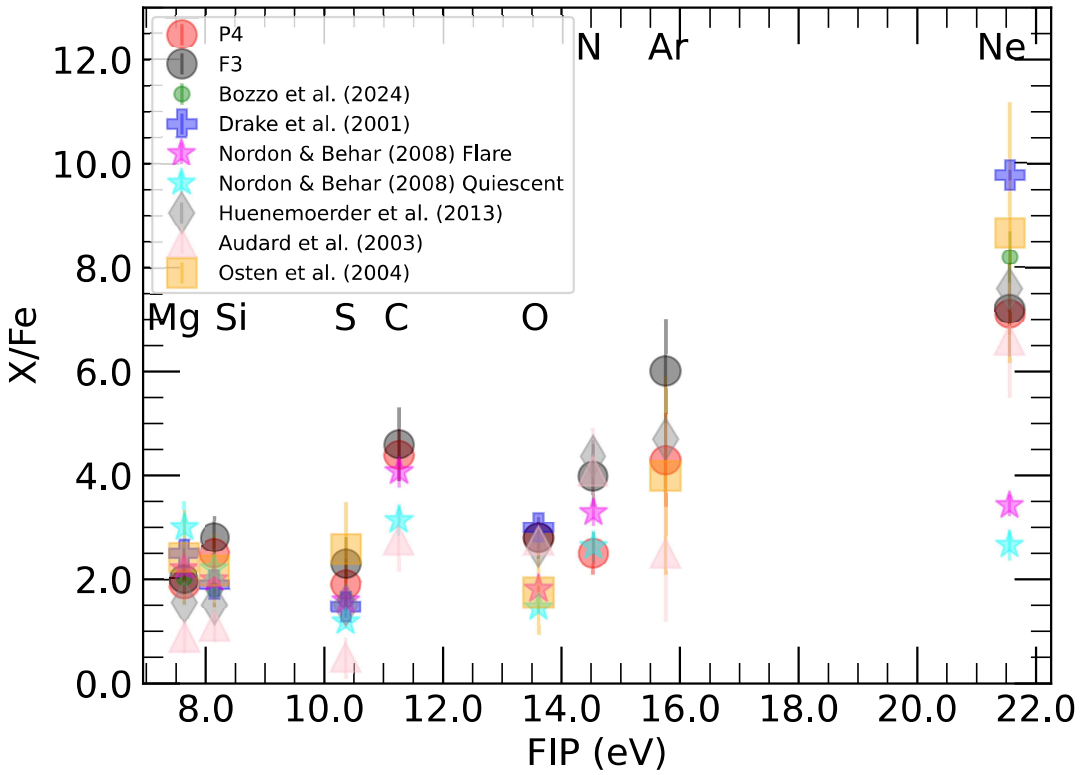

Figure 5.5: All the elemental abundances relative to Fe are plotted against the first ionization potential (FIP) for HR 1099. The values are provided in Table 5.2.

In contrast to solar corona, where low FIP elements show enhanced abundances with respect to high FIP elements (Feldman and Laming, 2000; Laming, 2015; von Steiger et al., 1995), the coronae of AB Dor and HR 1099 show the i-FIP effect. Such inverse FIP effect is found in active M dwarfs and active binaries (Brinkman et al., 2001; Liefke et al., 2008; Seli et al., 2022) and also has been reported for AB Dor by many authors in the past (Güdel et al., 2001; Lalitha et al., 2013; Maggio et al., 2000). An inverse-FIP effect near sunspots during flares has recently been detected for the first time (Doschek et al., 2015), which supports that the highly active region shows the I-FIP phenomenon. The FIP and i-FIP effects in the active stars have been explained in detail by Laming et al. (2019). The ponderomotive force associated with the Alfvén waves and fast mode waves separates ions from neutrals in the chromospheric regions, which can explain the physical mechanism responsible for such effects (Laming, 2021; To et al., 2021, and references

therein). The resonant Alfvén waves propagating along coronal loops can result in the FIP effect, while the i-FIP effect can be reasonably explained by upward-propagating p-modes. The magneto-acoustic waves or p-modes convert to fast modes and propagate into the low plasma beta (β < 1) regions (Baker et al., 2019; Laming, 2004, 2015, 2021). Such plasma processes can also be attributed as a physical cause of the FIP and i-FIP effects observed presently in the flaring epochs of the localized corona of AB Dor and HR 1099. The Solar-like FIP effects at older aged stars are noticed, whereas an inverse-FIP or no FIP effect has been found for the younger (<300 Myr) and most active stars (Telleschi et al., 2005). Further, it has been reported that there is a strong relationship between spectral class and FIP bias, with M dwarfs having an inverse-FIP effect that decreases to zero at a mid-K spectral type and subsequently drifts toward a solar-like FIP effect for early G dwarfs (Wood and Linsky, 2010; Wood et al., 2012). As AB Dor is a young and highly active K dwarf, and HR 1099 is K type giant, therefore, the I-FIP effect is expected. The Fe/O ratio can be used as a proxy to the extent of FIP bias in coronal abundances Wood and Linsky (2010). We found the $(Fe/O)_*$ abundance during the quiescent state ranges from 0.02 – 0.03 for AB Dor. The smaller value for the Fe/O abundance is indicative of a stronger I-FIP effect. The quiescent corona of AB Dor showed the I-FIP effect at nearly the same level for the time span of 19 years, which is longer than the photospheric activity cycle of AB Dor (see Güdel et al., 2001). It appears as if the fractionation process that is causing FIP bias in AB Dor is independent of the magnetic activity cycle of AB Dor. Furthermore, the I-FIP effect seems to remain the same or get weaker during the flaring epochs with $(Fe/O)_*$ abundance in the range of 0.02 – 0.04. For the strongest flare F15, the $(Fe/O)_*$ ratio is found to be a maximum of 0.04, indicating a weaker inverse FIP effect, whereas the overall abundances of each element increase during the flares due to the filling of dense plasma from chromospheric footpoints. One of the possibilities is that

the weakened inverse FIP effect is a result of a higher heating rate compared to magnetic energy, which, in turn, weakens the fractionation process.

In this study, we provide a comparative analysis of the coronal elemental abundances and the i-FIP effect in the coronal loop plasma of HR 1099 with the other estimations existing in the previous literature. The coronal abundances (Z/Z$\odot$) relative to Fe are presented in Table 5.2 and Fig. 5.5 for P4 and flare F3, alongside previously reported values obtained from various instruments. In this study, we assumed the photospheric values of HR 1099 to be analogous to those of the solar photosphere. Here, we assumed the photospheric values of HR 1099 to be analogous to those of the solar photosphere. The derived values of abundance are found to be consistent with the past literature values. However, the abundances of Fe and Ne as derived by Nordon and Behar (2007) exhibit lower values compared to those derived in other studies. The Fe and O abundances align closely with earlier reports, with minimal uncertainty, making the Fe/O ratio a useful indicator of the FIP bias in coronal abundances (Wood and Linsky, 2010; Wood et al., 2012). The Fe/O abundance ratio during the quiescent state P4 and flaring state F3 of HR 1099 were found to be 0.36±0.02 and 0.35±0.05, respectively. These values are consistent with previously reported values between 0.3 and 0.7 for HR 1099, as shown in Table 5.2. In other active RS CVn binaries, the Fe/O ratio varies based on the star's activity level and spectral type (UX Ari, λ And, VY Ari, Capella, etc; Audard et al., 2003; Nordon and Behar, 2007; Seli et al., 2022).

Table 5.2: Abundances of the elements with respect to Fe in the corona of HR 1099, along with the other observations taken from the literature. All the values are expressed relative to the solar photospheric abundances (Anders and Grevesse, 1989).

Elements(↓)	P4	F3	Z^a	Z^b	Z^c	Z^d	Z^e	Z^f
					Flare / Quiescent			
$[C/Fe]$	4.4±0.5	4.6±0.7	...	...	4.0±0.3 / 3.1±0.3	...	2.75±0.6	...
$[N/Fe]$	2.5±0.4	4.0±0.6	...	...	3.3±0.2 / 2.6±0.3	4.37±0.3	4.1±0.8	...
$[O/Fe]$	2.7±0.2	2.8±0.4	...	3±0.1	1.81±0.05 / 1.5±0.1	2.63±0.06	2.75±0.5	1.75±0.8
$[Ne/Fe]$	7.1±0.4	7.2±0.9	8.2±0.5	9.77±0.1	3.4±0.2 / 2.7±0.3	7.59±0.2	6.6±1.1	8.67±2.5
$[Mg/Fe]$	1.9±0.2	2.0±0.3	2.0±0.1	2.5±0.1	2.2±0.2 / 3.0±0.5	1.55±0.04	0.9±0.3	2.42±0.9
$[Si/Fe]$	2.5±0.3	2.8±0.4	1.8±0.1	1.9±0.1	2.0±0.1 / 2.2±0.4	1.51±0.04	1.1±0.3	2.17±0.7
$[S/Fe]$	1.9±0.5	2.3±0.5	1.6±0.2	1.48±0.2	1.6±0.1 / <1.2	1.51±0.07	0.5±0.4	2.58±0.9
$[Ar/Fe]$	4.3±0.9	6±1	...	...	... / ...	4.7±0.4	2.5±1.3	4.0±1.9

[a]Bozzo et al. (2024), [b]Drake et al. (2001), [c]Nordon and Behar (2008), [d] Huenemoerder et al. (2013), [e]Audard et al. (2003), [f]Osten et al. (2004)

Table 5.3: Best fit spectral parameters as obtained from the spectral fitting of RGS spectra of AB dor. All the parameters are quoted with a 68 per cent confidence interval.

Parameters (→) Segments (↓)	T_1 (keV)	T_2 (keV)	T_3 (keV)	EM_1 (10^{52} cm^{-3})	EM_2 (10^{52} cm^{-3})	EM_3 (10^{52} cm^{-3})	C	N	O	Ne	Mg	Si	S	Ar	Fe	L_{XF} (10^{30} erg s^{-1})	χ^2_ν(dof)
S2-P3	$0.28^{+0.01}_{-0.01}$	$0.76^{+0.03}_{-0.02}$	$1.7^{+0.2}_{-0.2}$	$1.9^{+0.2}_{-0.2}$	$4.2^{+0.4}_{-0.4}$	$3.9^{+0.3}_{-0.3}$	$0.7^{+0.1}_{-0.1}$	$0.7^{+0.1}_{-0.1}$	$0.37^{+0.04}_{-0.04}$	$1.2^{+0.1}_{-0.1}$	$0.22^{+0.08}_{-0.08}$	$0.3^{+0.1}_{-0.1}$	$0.2^{+0.1}_{-0.1}$	$0.9^{+0.3}_{-0.3}$	$0.17^{+0.02}_{-0.02}$	$1.07^{+0.01}_{-0.01}$	1.31 (434)
F4	-	-	$1.66^{+0.1}_{-0.08}$	-	-	$4.1^{+0.2}_{-0.2}$	$0.87^{+0.09}_{-0.09}$	$0.73^{+0.09}_{-0.09}$	$0.39^{+0.01}_{-0.01}$	$1.39^{+0.08}_{-0.08}$	$0.32^{+0.07}_{-0.07}$	$0.3^{+0.1}_{-0.1}$	$0.5^{+0.1}_{-0.1}$	$0.7^{+0.2}_{-0.2}$	$0.182^{+0.006}_{-0.006}$	$1.14^{+0.01}_{-0.01}$	1.34 (583)
F5	-	-	$1.8^{+0.2}_{-0.1}$	-	-	$2.7^{+0.1}_{-0.1}$	$0.81^{+0.07}_{-0.07}$	$0.49^{+0.06}_{-0.06}$	$0.39^{+0.01}_{-0.01}$	$1.29^{+0.06}_{-0.06}$	$0.29^{+0.06}_{-0.06}$	$0.27^{+0.07}_{-0.07}$	$0.34^{+0.07}_{-0.07}$	$0.8^{+0.1}_{-0.1}$	$0.175^{+0.004}_{-0.004}$	$0.973^{+0.007}_{-0.007}$	1.60 (811)
P4	$0.30^{+0.01}_{-0.02}$	$0.73^{+0.02}_{-0.03}$	$1.8^{+0.4}_{-0.3}$	$1.6^{+0.2}_{-0.2}$	$3.1^{+0.4}_{-0.3}$	$2.1^{+0.2}_{-0.2}$	$0.9^{+0.2}_{-0.2}$	$0.7^{+0.1}_{-0.1}$	$0.45^{+0.04}_{-0.04}$	$1.5^{+0.2}_{-0.1}$	$0.37^{+0.09}_{-0.08}$	$0.6^{+0.1}_{-0.1}$	$0.6^{+0.2}_{-0.1}$	$1.1^{+0.3}_{-0.3}$	$0.19^{+0.02}_{-0.02}$	$0.811^{+0.008}_{-0.008}$	1.31 (471)
F6	-	-	$1.9^{+0.2}_{-0.1}$	-	-	$6.3^{+0.3}_{-0.3}$	$0.9^{+0.1}_{-0.1}$	$0.6^{+0.1}_{-0.1}$	$0.35^{+0.02}_{-0.02}$	$1.2^{+0.1}_{-0.1}$	$0.6^{+0.1}_{-0.1}$	$0.8^{+0.2}_{-0.2}$	$0.6^{+0.2}_{-0.2}$	$0.9^{+0.3}_{-0.3}$	$0.199^{+0.008}_{-0.008}$	$1.38^{+0.02}_{-0.02}$	1.14 (348)
F7	-	-	$1.94^{+0.09}_{-0.07}$	-	-	$10.2^{+0.2}_{-0.2}$	$0.75^{+0.07}_{-0.07}$	$0.64^{+0.07}_{-0.07}$	$0.35^{+0.01}_{-0.01}$	$1.16^{+0.06}_{-0.06}$	$0.24^{+0.06}_{-0.06}$	$0.45^{+0.09}_{-0.09}$	$0.11^{+0.08}_{-0.08}$	$1.1^{+0.1}_{-0.1}$	$0.180^{+0.005}_{-0.005}$	$1.65^{+0.01}_{-0.01}$	1.19 (1041)
F8	-	-	$1.92^{+0.09}_{-0.06}$	-	-	$15.0^{+0.3}_{-0.3}$	$0.89^{+0.09}_{-0.09}$	$0.7^{+0.1}_{-0.1}$	$0.41^{+0.01}_{-0.01}$	$1.30^{+0.08}_{-0.08}$	$0.30^{+0.07}_{-0.07}$	$0.6^{+0.1}_{-0.1}$	$0.4^{+0.1}_{-0.1}$	$1.1^{+0.2}_{-0.2}$	$0.220^{+0.007}_{-0.007}$	$2.25^{+0.01}_{-0.01}$	1.20 (971)
F9	-	-	$1.87^{+0.1}_{-0.09}$	-	-	$19.9^{+0.6}_{-0.6}$	$1.1^{+0.2}_{-0.2}$	$0.6^{+0.2}_{-0.2}$	$0.41^{+0.02}_{-0.02}$	$1.2^{+0.1}_{-0.1}$	$0.3^{+0.1}_{-0.1}$	$0.5^{+0.2}_{-0.2}$	$0.3^{+0.2}_{-0.2}$	$1.5^{+0.4}_{-0.4}$	$0.27^{+0.01}_{-0.01}$	$2.81^{+0.03}_{-0.03}$	1.19 (425)
S3-P5	$0.294^{+0.004}_{-0.004}$	$0.75^{+0.01}_{-0.01}$	$1.61^{+0.05}_{-0.03}$	$1.94^{+0.09}_{-0.08}$	$3.6^{+0.1}_{-0.1}$	$4.4^{+0.1}_{-0.1}$	$0.77^{+0.05}_{-0.05}$	$0.59^{+0.05}_{-0.04}$	$0.39^{+0.01}_{-0.01}$	$1.14^{+0.04}_{-0.04}$	$0.34^{+0.03}_{-0.03}$	$0.39^{+0.04}_{-0.04}$	$0.37^{+0.05}_{-0.05}$	$0.70^{+0.09}_{-0.09}$	$0.205^{+0.008}_{-0.007}$	$1.105^{+0.004}_{-0.004}$	1.46 (1923)
F10	-	-	$1.7^{+0.2}_{-0.1}$	-	-	$9.0^{+0.4}_{-0.4}$	$0.8^{+0.2}_{-0.2}$	$0.3^{+0.1}_{-0.1}$	$0.44^{+0.03}_{-0.03}$	$1.2^{+0.1}_{-0.1}$	$0.3^{+0.1}_{-0.1}$	$0.3^{+0.2}_{-0.2}$	$1.0^{+0.3}_{-0.3}$	$1.5^{+0.5}_{-0.5}$	$0.161^{+0.008}_{-0.008}$	$1.58^{+0.02}_{-0.02}$	1.18 (363)
S4-F11	-	-	$1.75^{+0.07}_{-0.09}$	-	-	$8.7^{+0.2}_{-0.2}$	$0.9^{+0.1}_{-0.1}$	$0.7^{+0.1}_{-0.1}$	$0.48^{+0.02}_{-0.02}$	$1.20^{+0.08}_{-0.09}$	$0.29^{+0.07}_{-0.07}$	$0.4^{+0.1}_{-0.1}$	$0.6^{+0.2}_{-0.2}$	$1.4^{+0.3}_{-0.3}$	$0.206^{+0.006}_{-0.006}$	$1.51^{+0.01}_{-0.01}$	1.12 (707)
P6	$0.28^{+0.01}_{-0.01}$	$0.70^{+0.01}_{-0.01}$	$1.68^{+0.09}_{-0.06}$	$1.5^{+0.1}_{-0.1}$	$3.8^{+0.2}_{-0.2}$	$5.1^{+0.2}_{-0.2}$	$0.86^{+0.09}_{-0.09}$	$0.59^{+0.07}_{-0.07}$	$0.44^{+0.02}_{-0.02}$	$1.20^{+0.07}_{-0.07}$	$0.36^{+0.05}_{-0.05}$	$0.32^{+0.07}_{-0.07}$	$0.5^{+0.1}_{-0.1}$	$1.2^{+0.2}_{-0.2}$	$0.17^{+0.01}_{-0.01}$	$1.134^{+0.007}_{-0.007}$	1.14 (1111)
F12	-	-	$1.69^{+0.09}_{-0.05}$	-	-	$8.9^{+0.2}_{-0.2}$	$0.6^{+0.1}_{-0.1}$	$0.9^{+0.1}_{-0.1}$	$0.47^{+0.02}_{-0.02}$	$1.36^{+0.08}_{-0.08}$	$0.33^{+0.07}_{-0.07}$	$0.4^{+0.1}_{-0.1}$	$0.5^{+0.1}_{-0.1}$	$1.1^{+0.3}_{-0.3}$	$0.209^{+0.006}_{-0.006}$	$1.54^{+0.01}_{-0.01}$	1.09 (717)
F13	-	-	$2.1^{+0.2}_{-0.2}$	-	-	$11.1^{+0.4}_{-0.4}$	$1.1^{+0.2}_{-0.2}$	$0.6^{+0.2}_{-0.2}$	$0.49^{+0.03}_{-0.03}$	$1.4^{+0.1}_{-0.1}$	$0.3^{+0.1}_{-0.1}$	$0.50^{+0.2}_{-0.2}$	$0.7^{+0.3}_{-0.3}$	$0.6^{+0.5}_{-0.5}$	$0.200^{+0.009}_{-0.009}$	$1.75^{+0.02}_{-0.02}$	1.12 (405)
P7	$0.29^{+0.01}_{-0.01}$	$0.70^{+0.02}_{-0.02}$	$1.59^{+0.1}_{-0.09}$	$1.3^{+0.2}_{-0.2}$	$3.8^{+0.3}_{-0.3}$	$4.6^{+0.3}_{-0.3}$	$1.1^{+0.2}_{-0.1}$	$0.6^{+0.1}_{-0.1}$	$0.47^{+0.04}_{-0.04}$	$1.4^{+0.1}_{-0.1}$	$0.24^{+0.07}_{-0.07}$	$0.6^{+0.1}_{-0.1}$	$0.4^{+0.2}_{-0.2}$	$1.3^{+0.4}_{-0.3}$	$0.17^{+0.02}_{-0.02}$	$1.10^{+0.01}_{-0.01}$	1.24 (510)
F14	-	-	$1.69^{+0.09}_{-0.05}$	-	-	$6.3^{+0.2}_{-0.2}$	$1.0^{+0.1}_{-0.1}$	$0.78^{+0.09}_{-0.09}$	$0.49^{+0.01}_{-0.01}$	$1.42^{+0.07}_{-0.07}$	$0.34^{+0.06}_{-0.06}$	$0.37^{+0.08}_{-0.08}$	$1.0^{+0.1}_{-0.1}$	$1.2^{+0.2}_{-0.2}$	$0.196^{+0.005}_{-0.005}$	$1.324^{+0.009}_{-0.009}$	1.13 (935)
S5-P8	$0.297^{+0.009}_{-0.01}$	$0.76^{+0.03}_{-0.02}$	$1.6^{+0.1}_{-0.1}$	$2.1^{+0.2}_{-0.2}$	$3.5^{+0.3}_{-0.2}$	$4.0^{+0.2}_{-0.2}$	$0.9^{+0.1}_{-0.1}$	$0.9^{+0.1}_{-0.1}$	$0.44^{+0.04}_{-0.03}$	$1.3^{+0.1}_{-0.1}$	$0.29^{+0.07}_{-0.07}$	$0.5^{+0.1}_{-0.1}$	$0.8^{+0.2}_{-0.2}$	$0.6^{+0.2}_{-0.2}$	$0.22^{+0.02}_{-0.02}$	$1.134^{+0.007}_{-0.007}$	1.22 (596)
F15	-	-	$4.94^{+0.07}_{-0.07}$	-	-	$120.6^{+0.7}_{-0.7}$	$2.4^{+0.1}_{-0.1}$	$1.6^{+0.1}_{-0.1}$	$1.12^{+0.02}_{-0.02}$	$3.00^{+0.08}_{-0.08}$	$0.72^{+0.09}_{-0.09}$	$0.7^{+0.1}_{-0.1}$	$2.7^{+0.2}_{-0.2}$	$3.4^{+0.4}_{-0.4}$	$0.90^{+0.01}_{-0.01}$	$15.05^{+0.03}_{-0.03}$	1.59 (3111)
F16	-	-	$1.91^{+0.1}_{-0.08}$	-	-	$12.5^{+0.6}_{-0.5}$	$1.7^{+0.4}_{-0.3}$	$1.3^{+0.3}_{-0.3}$	$0.96^{+0.05}_{-0.05}$	$2.6^{+0.2}_{-0.2}$	$0.6^{+0.2}_{-0.1}$	$0.6^{+0.2}_{-0.2}$	$0.7^{+0.4}_{-0.4}$	$1.5^{+0.7}_{-0.6}$	$0.44^{+0.02}_{-0.02}$	$2.51^{+0.03}_{-0.03}$	1.13 (3110)
P9	$0.294^{+0.004}_{-0.004}$	$0.74^{+0.01}_{-0.01}$	$1.69^{+0.04}_{-0.03}$	$1.53^{+0.06}_{-0.06}$	$3.23^{+0.09}_{-0.09}$	$4.72^{+0.08}_{-0.08}$	$0.86^{+0.05}_{-0.05}$	$0.70^{+0.04}_{-0.04}$	$0.45^{+0.01}_{-0.01}$	$1.38^{+0.04}_{-0.04}$	$0.38^{+0.03}_{-0.03}$	$0.31^{+0.04}_{-0.04}$	$0.49^{+0.05}_{-0.05}$	$0.81^{+0.09}_{-0.09}$	$0.202^{+0.006}_{-0.006}$	$1.10^{+0.01}_{-0.01}$	1.39 (2282)
S6-F17	-	-	$1.71^{+0.09}_{-0.08}$	-	-	$5.5^{+0.2}_{-0.2}$	$1.4^{+0.2}_{-0.2}$	$0.8^{+0.1}_{-0.1}$	$0.54^{+0.02}_{-0.02}$	$1.28^{+0.08}_{-0.09}$	$0.40^{+0.08}_{-0.08}$	$0.4^{+0.1}_{-0.1}$	$0.6^{+0.2}_{-0.2}$	$0.8^{+0.3}_{-0.3}$	$0.208^{+0.007}_{-0.007}$	$1.20^{+0.01}_{-0.01}$	1.19 (531)
F18	-	-	$1.88^{+0.09}_{-0.08}$	-	-	$6.6^{+0.2}_{-0.2}$	$1.3^{+0.2}_{-0.1}$	$0.7^{+0.1}_{-0.1}$	$0.53^{+0.02}_{-0.02}$	$1.25^{+0.07}_{-0.07}$	$0.29^{+0.07}_{-0.07}$	$0.5^{+0.1}_{-0.1}$	$0.4^{+0.1}_{-0.1}$	$0.9^{+0.2}_{-0.2}$	$0.213^{+0.006}_{-0.006}$	$1.29^{+0.01}_{-0.01}$	1.11 (822)
P11	$0.302^{+0.02}_{-0.008}$	$0.76^{+0.03}_{-0.01}$	$2.3^{+0.3}_{-0.2}$	$1.5^{+0.2}_{-0.1}$	$3.0^{+0.2}_{-0.2}$	$3.4^{+0.2}_{-0.2}$	$1.1^{+0.2}_{-0.1}$	$0.7^{+0.1}_{-0.1}$	$0.53^{+0.04}_{-0.03}$	$1.6^{+0.1}_{-0.1}$	$0.31^{+0.07}_{-0.07}$	$0.3^{+0.1}_{-0.1}$	$0.6^{+0.1}_{-0.1}$	$0.5^{+0.2}_{-0.2}$	$0.19^{+0.02}_{-0.01}$	$0.962^{+0.005}_{-0.005}$	1.18 (749)
F19	-	-	$1.79^{+0.1}_{-0.07}$	-	-	$8.8^{+0.3}_{-0.3}$	$0.9^{+0.2}_{-0.2}$	$0.8^{+0.2}_{-0.2}$	$0.46^{+0.02}_{-0.02}$	$1.3^{+0.1}_{-0.1}$	$0.5^{+0.1}_{-0.1}$	$0.6^{+0.1}_{-0.1}$	$0.8^{+0.2}_{-0.2}$	$0.5^{+0.3}_{-0.3}$	$0.250^{+0.009}_{-0.009}$	$1.6^{+0.01}_{-0.01}$	0.95 (509)
F20	-	-	$2.78^{+0.05}_{-0.05}$	-	-	$32.4^{+0.2}_{-0.2}$	$1.3^{+0.1}_{-0.1}$	$0.93^{+0.08}_{-0.08}$	$0.72^{+0.01}_{-0.01}$	$2.13^{+0.06}_{-0.06}$	$0.50^{+0.06}_{-0.06}$	$0.51^{+0.08}_{-0.08}$	$1.0^{+0.1}_{-0.1}$	$1.4^{+0.2}_{-0.2}$	$0.457^{+0.006}_{-0.006}$	$4.32^{+0.01}_{-0.01}$	1.42 (2440)
F21	-	-	$1.9^{+0.1}_{-0.1}$	-	-	$7.0^{+0.2}_{-0.2}$	$1.2^{+0.2}_{-0.2}$	$0.7^{+0.1}_{-0.1}$	$0.61^{+0.02}_{-0.02}$	$1.59^{+0.09}_{-0.09}$	$0.45^{+0.09}_{-0.08}$	$0.6^{+0.1}_{-0.1}$	$0.4^{+0.2}_{-0.2}$	$0.7^{+0.3}_{-0.3}$	$0.251^{+0.007}_{-0.007}$	$1.44^{+0.01}_{-0.01}$	1.21 (682)